ELSEVIER

Versatility of infrared properties of MXenes

Meikang Han [1,2,*,#], Danzhen Zhang [1,#], Akash Singh [3,#], Tetiana Hryhorchuk [1], Christopher Eugene Shuck [1], Teng Zhang [1], Lingyi Bi [1], Bernard McBride [1], Vivek B. Shenoy [3], Yury Gogotsi [1,*]

[1] A. J. Drexel Nanomaterials Institute and Department of Materials Science and Engineering, Drexel University, Philadelphia, PA 19104, USA
[2] Institute of Optoelectronics and Shanghai Frontiers Science Research Base of Intelligent Optoelectronics and Perception, Fudan University, Shanghai 200433, China
[3] Department of Materials Science and Engineering, University of Pennsylvania, Philadelphia, PA 19104, USA

Selective and ultrathin films and coatings capable of controlling infrared (IR) emission are crucial for highly integrated thermal management systems, but are challenging produce using conventional materials. Here, we report that the MXene family of two-dimensional carbides and carbonitrides offers a broad range of IR emissivity values (~0.06–0.59) with diverse colors, varying with MXene composition and structure. Specifically, 200 nm thick purple $Ti_3C_2T_x$ coating has an average IR emissivity of 0.06, while gold Nb_2CT_x coating is 0.59 at wavelengths from 3-25 μm. We demonstrate that the IR emissivity can be finely tuned by combining different metals in solid-solution MXenes. Furthermore, the IR identification capability at varying temperatures was validated using different MXene coatings and patterned MXene fabrics. The versatility of MXenes at optical and infrared wavelengths provides a platform for developing MXene-based smart, flexible devices and wearables capable of selective and localized thermal management, aiming at radiative heating/cooling, IR identification, photothermal conversion, and thermal imaging.

Keywords: MXene; Infrared emissivity; Infrared radiation; Thermal management; Patterned fabric

Introduction

Thermal management is ubiquitous in human activities, from integrated electronics to spacecrafts, and from everyday clothes we wear to the buildings we live in. The control of consequent energy consumption is challenging, in spite of various thermal management technologies being developed. In contrast to external energy modulation (e.g., air-conditioning), radiative thermal management is a passive process with low/zero heat waste, which is capable of regulating the temperature and improving the energy exchange efficiency between objects with different temperatures at no additional energy cost [1–5].

For passive heat management, low infrared (IR) emission/absorption is required to suppress radiative energy loss by Stefan-Boltzmann's law. Conventional polished metals (Al, Ag, Au, etc.) have ultralow IR emissivity (<0.1). Typically, thin metal coatings are deposited using magnetron sputtering or electroless plating, especially for complex architectures [6]. While they have low IR emissivity, their high thermal conductivity limits their efficiency, requiring additional thermal insulation. Conversely, for radiative cooling, materials are expected to be IR-transparent (high IR emissivity), primarily within the atmospheric window (8–14 μm), allowing thermal radiation to bypass

* Corresponding authors.
E-mail addresses: Han, M. (mkhan@fudan.edu.cn), Gogotsi, Y. (gogotsi@drexel.edu).
# These authors contributed equally to this work.

 https://doi.org/10.1016/j.mattod.2023.02.024

the barrier perpetually. Currently, the state of the art in adaptive radiation heating/cooling uses metamaterials to manipulate the phonon behavior in the IR range [7], including topological transitions, photonic crystals, epsilon-near-zero surfaces, and others [8–10]. However, the difficulty in manufacturing these complex structures limits their applications in highly integrated devices and large-scale thermal manipulation components due to cost and scalability issues. Alternative approaches, such as active electrical modulation of thermal emissivity, are promising, but have limited range and rely on the inherent thermal properties of the structures [11,12]. Therefore, achieving selective thermal radiation using passive intrinsic IR emission material characteristics remains challenging.

Two-dimensional transition metal carbides and nitrides (MXenes) have shown diverse light-matter interactions in a broad frequency range [13,14], owing to their highly anisotropic electronic and optical properties, easy-to-functionalize surfaces, and high density of states at the Fermi level [15–18]. For instance, MXenes present transverse surface plasmon resonances from the ultraviolet (UV) to near-IR (NIR) range as a function of structure and composition [19]. They also strongly interact with electromagnetic waves from terahertz to gigahertz frequency [20–22]. There are a few reports on light-to-heat conversion of $Ti_3C_2T_x$ MXene for thermal management [23–27]. However, little is known about the intrinsic thermal radiation properties of different MXenes, especially in the IR range at different temperatures. On top of that, more than 30 kinds of stoichiometric MXenes have been experimentally synthesized, with numerous MXene compositions theoretically predicted, but the optical properties of a fraction of the family have been reported [23,28–32]. It is likely that MXenes have diverse IR radiation properties depending on the composition, atomic arrangement, and surface chemistry. Moreover, due to the solution processability of MXenes, thin MXene films/coatings from nanometer- to micrometer-thickness can be readily manufactured using multiple scalable techniques [33,34]. The ease of processing coupled with the natural hydrophilicity and flexibility of MXenes facilitates the deposition of MXenes on a wide variety of surfaces, enabling fast and easy coating of surfaces for thermal management, such as selective heating/cooling, IR camouflage, thermal circuits, smart textiles, and others [35,36].

Herein, we report the broad IR emission range of 10 different MXenes, covering all typical MXene structures, and demonstrate the potential of MXenes for object identification/camouflage and other thermal management applications. The intrinsic IR emissivity of MXene films at room and high temperatures was experimentally investigated and theoretically calculated. The effects of temperature, thickness, roughness, and electrical conductivity on IR emission provide insights into the tunability of thermal radiation from MXenes. The IR radiation performance was validated through IR imaging of MXene coatings and MXene-patterned cotton fabrics, demonstrating IR identification capability with various MXenes. This work not only illustrates the potential use of MXenes (e.g., $Ti_3C_2T_x$, Ti_3CNT_x, and $V_4C_3T_x$) in IR camouflage and radiation heating but also paves the road to selective and localized thermal management using MXenes. Moreover, the combination of diverse optical and IR radiation properties makes MXene coatings available for both energy-saving and aesthetical demands.

Results and discussion

MXene structures and coatings

Ten different MXenes, which cover typical MXene structures and compositions, were synthesized, including single-M MXenes (M_2CT_x: Ti_2CT_x, Nb_2CT_x, and V_2CT_x; $M_3C_2T_x$: $Ti_3C_2T_x$; $M_4C_3T_x$: $V_4C_3T_x$ and $Nb_4C_3T_x$), solid solution MXenes ($MM'CT_x$: $Ti_{1.6}Nb_{0.4}CT_x$ and $Ti_{0.4}Nb_{1.6}CT_x$; M_3CNT_x: Ti_3CNT_x), and an in-plane ordered double-metal MXene ($M_2M'_2C_3T_x$: $Mo_2Ti_2C_3T_x$) (Fig. 1). All MXenes were produced by etching the corresponding MAX phases (Fig. S1a) and subsequent delamination. After delamination, few-layer flakes with sizes dependent on the MXene composition were obtained (Fig. S2). The MXenes were spray-coated onto glass substrates from the colloidal solutions. Each MXene coating looks different visually and under optical microscope (Fig. 1 and Fig. S3), indicating the diversity of optical properties [19]. For example, Ti_2CT_x is green, $Ti_3C_2T_x$ is purple, $Mo_2Ti_2C_3T_x$ is silvery, and Nb_2CT_x has a golden color. This feature, coupled with their infrared properties renders the MXene family unique for photothermal and imaging applications, which will be discussed later. MXene coatings have smooth surfaces with a roughness range of 18–33 nm (Fig. S4), eliminating the influence of surface condition on the IR emission measurements. The cross-section of MXene film shows well-aligned layers (Fig. S5). X-ray diffraction (XRD) patterns of MXene films show (002) diffraction peaks from 4.8°-7.6° (2θ), further confirming the complete etching and delamination (Fig. S1b). It is noteworthy that the *d*-spacing values are related to both the MXene layers (*n*) and the intercalants. For example, thicker $M_4C_3T_x$ ($V_4C_3T_x$, $Nb_4C_3T_x$, and $Mo_2Ti_2C_3T_x$) films have a larger *d*-space than other MXenes due to a larger number of atomic layers. The *d*-spacing of Ti_2CT_x is 11.62 Å whereas V_2CT_x is 12.98 Å. This is ascribed to Li^+ intercalation of Ti_2CT_x and TMA^+ intercalation of V_2CT_x.

Infrared emission of MXenes

According to Kirchhoff's law, the emissivity (ε) of homogeneous films with smooth surface is equal to the absorptivity in thermal equilibrium state (Fig. 2a). The emissivity spectra of MXene coatings at room temperature were obtained by measuring the reflectance with a Fourier transform infrared (FTIR) spectrometer over a wavelength range of 1–25 μm (Fig. 2b). The emissivity of all MXenes decreases with the increasing wavelength. The average infrared emissivity (3–25 μm) values are 0.06 for $Ti_3C_2T_x$ and 0.59 for Nb_2CT_x, respectively, whereas the values of other MXenes fall in between. Ti_3CNT_x, V_2CT_x, $V_4C_3T_x$, Ti_2CT_x, $Ti_{1.6}Nb_{0.4}CT_x$, and $Mo_2Ti_2C_3T_x$ coatings also exhibit low emissivity (<0.5) at 3–25 μm, which is capable of suppressing thermal radiation for radiative heating. Particularly, the ultralow IR emissivity value of the $Ti_3C_2T_x$ coating is attributed to its high free electron concentration and mobility. In addition, these MXenes show a dramatic drop of emissivity around 2.5 μm, indicating the selectivity of IR radiation from NIR to mid-IR range. Meanwhile, Nb-based MXenes ($Nb_4C_3T_x$, Nb_2CT_x, and $Ti_{0.4}Nb_{1.6}CT_x$) show relatively high emissivity (>0.5). Notably, the emissivity

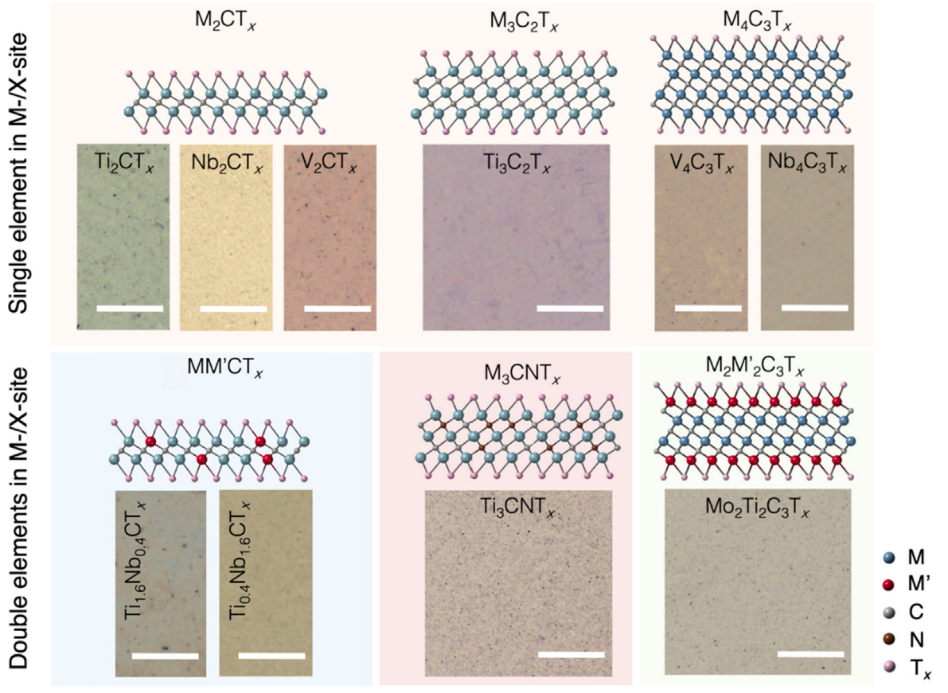

FIGURE 1

Wide range of MXene coatings. Schematics of atomic structures of MXenes, showing three representative types of MXenes (M_2XT_x, $M_3X_2T_x$, and $M_4X_3T_x$). They can also be sorted into two kinds depending on the element composition and arrangement: single element in M-/X-site and double elements in M-/X-site (solid solution and ordered in-plane structure). Optical images of MXene coatings show their different perceived colors and smooth surfaces. Scale bar, 20 μm.

increases with the mass ratio of Nb, when comparing solid solution MXenes ($Ti_{1.6}Nb_{0.4}CT_x$ and $Ti_{0.4}Nb_{1.6}CT_x$) with Ti_2CT_x and Nb_2CT_x. It indicates that the infrared properties are tunable through the M−site substitution in continuous solid-solution MXenes. The emissivity can be further optimized with different etching and intercalation processes. The wide variety of MXenes emissivity values reveals that selective infrared emission can be achieved with different MXene compositions.

To better characterize the effect of MXene composition, we plotted the average emissivity at two IR atmospheric windows (3–5 μm and 8–14 μm) as a function of the electrical conductivity of the MXene coatings (Fig. 2c and Fig. S6). They exhibit a conductivity-dependent behavior whereby the emissivity increases with decreasing conductivity. The correlation of IR emissivity with the conductivity is similar to metal films [37] and allows us to attribute low emissivity to the metallic character of MXenes. However, given that an indirect measurement was used and MXenes are 2D materials with varying surface groups, diffraction and other near-field effects in thermal radiation of MXenes need to be explored further [38].

We summarized the IR emission performance of MXene coatings and other thin films with low IR emissivity (details are provided in Table S1). Metal films have ultralow emissivity with a thickness of < 1 μm, while transparent conductive oxide films (ITO: indium tin oxide film; AZO: Al-doped zinc oxide film) show higher values (Fig. 2d). Remarkably, ~200 nm thick $Ti_3C_2T_x$ coating has a competitive performance with gold film and outperforms others. In contrast to magnetron sputtering process of noble metal films, solution-processable and ultrathin MXene films are available for more scenarios. For example, MXene paint can be used for the building thermal envelope to regulate indoor temperature. MXenes can also be easily integrated with complex devices using various coating techniques. The large-scale synthesis of MXene demonstrates the possibility of commercial use outside of the laboratory. Moreover, colored MXene films satisfy the aesthetical effect while metal films commonly suffer from silver color. More broadly, the diverse IR radiation of MXenes, covering both low-emission and high-emission materials, provides a larger room for thermal manipulation.

To visualize low IR emissivity of $Ti_3C_2T_x$, Ti_3CNT_x, and $V_4C_3T_x$, MXene-coated slides were placed onto a hot plate heated to 110 °C for 300 s with the exterior temperature measured using an IR camera. For all three MXenes, the temperature increased rapidly in the first 30 s, and then stabilized after ~ 300 s (Fig. 2e). In contrast to the background temperature, the temperature difference of $Ti_3C_2T_x$ and Ti_3CNT_x reaches 70.5 °C and 66 °C, respectively, and attributed to their ultralow IR emission. Since $V_4C_3T_x$ has a higher emissivity, it exhibited a smaller temperature change of 43.7 °C after 300 s. From the IR images of MXene coatings on a hot plate (Fig. S7), the temperature change of different MXene coatings with increasing time was visually observed. $Ti_3C_2T_x$ and Ti_3CNT_x coatings have no extreme temperature change upon heating, while $V_4C_3T_x$ shows a change from 57.0 to 66.3 °C. We further investigated the thermal radiation behavior of $Ti_3C_2T_x$ films with different coating thicknesses (~200, 600, and 1300 nm). The three coatings show a similar IR emissivity (Fig. 2f), which leads to 71.7 °C temperature changes for the 1300 nm thick $Ti_3C_2T_x$ coating, and 70.8 °C for the

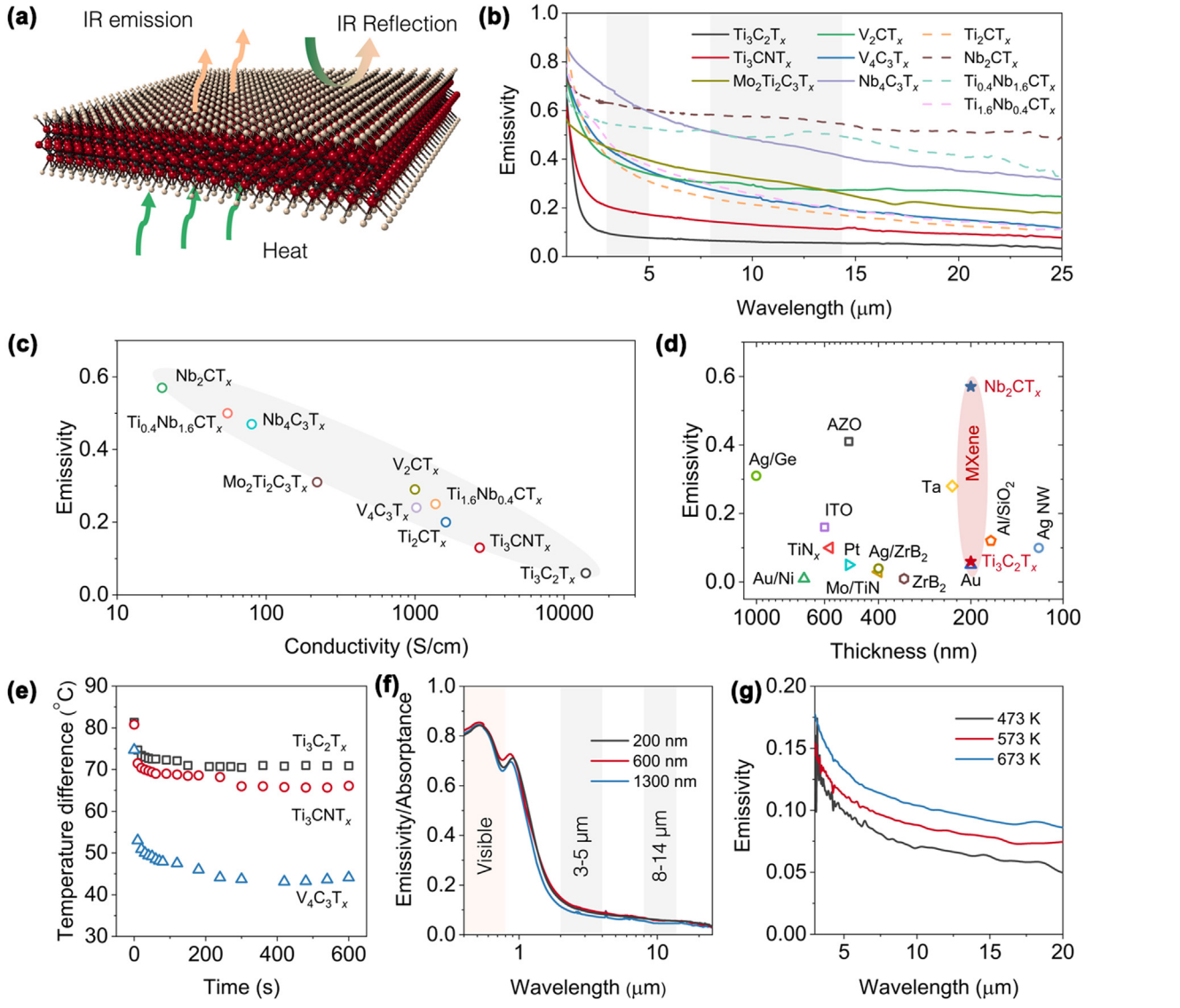

FIGURE 2

Infrared emission capability of MXenes. (a) Schematic of IR reflection and emission with MXene. (b) The room-temperature IR emissivity spectra of MXene coatings at a range of 1–25 μm. Dash lines show the comparison of solid solution MXenes. The shadows show the two atmospheric windows. (c) The relationship between the average infrared emissivity (8–14 μm) and electrical conductivity of MXene coatings. (d) IR emissivity versus thickness of MXene films and other films reported in the literature, including metal films and transparent conductive films. Ag NW: Ag nanowire. (e) Temperature difference between MXene coating and background as a function of time for different MXene coatings ($Ti_3C_2T_x$, Ti_3CNT_x, and $V_4C_3T_x$) with a thickness of ~ 200 nm on a hot plate at 110 °C. (f) Emissivity/absorptance of $Ti_3C_2T_x$ coatings with different thicknesses (~200 nm, ~600 nm, and ~ 1300 nm) at a range of 0.4–25 μm. (g) The infrared emissivity spectra of $Ti_3C_2T_x$ coating at elevated temperature (473–673 K).

200 nm coating (Fig. S8). Moreover, it is noteworthy that $Ti_3C_2T_x$ has ultralow IR emissivity but high solar absorptance (Fig. 2f), implying the potential in selective energy conversion applications.

The comprehensive IR radiation performance of MXenes was explored by recording the IR emissivity spectra (3–25 μm) of MXene coatings at high temperatures (473–673 K) with a direct radiation process (Fig. 2g and Fig. S9). The emissivity values of all MXenes increase with the increasing temperature except for Nb-based MXenes (Nb_2CT_x and $Ti_{0.4}Nb_{1.6}CT_x$; Figs. S9c and S9h). For example, the average emissivity values of $Ti_3C_2T_x$ and Ti_3CNT_x increase from 0.09 (473 K) to 0.13 (673 K), and from 0.23 (473 K) to 0.26 (673 K), respectively. This is attributed to the stronger vibration with the increasing temperature, leading to stronger absorption for IR photons. For the anomalous behavior in Nb-based MXenes, although they are also metallic, it might be related to the intercalants between layers. For V-based MXenes (V_2CT_x and $V_4C_3T_x$), several absorption peaks appear when the temperature reaches 673 K. This is ascribed to the oxidation of these MXenes at high temperature in air, which was confirmed by Raman spectroscopy. Both the peaks (145 cm^{-1} and 996 cm^{-1}) of V_2O_5 and the broad carbon peaks (~1336 cm^{-1} and ~ 1590 cm^{-1}) appear after annealing $V_4C_3T_x$ at 673 K [39]. However, there are no changes in Raman spectra of $Ti_3C_2T_x$ and Ti_3CNT_x after annealing, which indicates the superior thermal stability of Ti-based MXenes, making them

promising for high-temperature thermal management. In addition, the variation of emissivity with temperature depends on the MXene composition. For example, the emissivity of $Mo_2Ti_2C_3T_x$ shows no significant temperature dependence but a wavelength-dependent behavior. Further investigation is required to quantify the phonon excitation of different MXenes for better understanding their IR radiation as a function of temperature.

Theoretical calculations

To better understand the effects of composition and structure on the optical/IR absorption of MXenes, theoretical calculations were conducted for four MXenes (Nb_2C, V_2C, V_4C_3, and Ti_3C_2) using the hybrid density functional theory (DFT). We calculated the real (ε_1) and imaginary (ε_2) parts of the dielectric function with the photon frequency (ω) for bare Nb_2C, V_2C, V_4C_3, and Ti_3C_2 (Fig. 3a-3b and Fig. S11) [40]. The optical absorption (α) spectrum, which is defined in the independent-particle approximation (IPA), is proportional to the imaginary component of the frequency-dependent dielectric function [$\varepsilon(\omega) = \varepsilon_1(\omega) + i\varepsilon_2(\omega)$] and defined as [41];

$$\varepsilon_2(\omega) = \frac{8\pi^2 e^2}{V} \sum_k |d_k|^2 \delta(\omega - \Delta\varepsilon_k) \quad (1)$$

where d_κ is the transition energy of the electrons that absorbs the entering electromagnetic field with frequency (ω) and $\Delta\varepsilon_\kappa$ is the dipole matrix element.

The material's surface light reflection ($r(\omega)$) at normal incidence can be determined by

$$r(\omega) = \left| \frac{\sqrt{\varepsilon_1(\omega) + i\,\varepsilon_2(\omega)} - 1}{\sqrt{\varepsilon_1(\omega) + i\,\varepsilon_2(\omega)} + 1} \right|^2 \quad (2)$$

Optical absorption of any optically dense material that has no transmission can be described by equation:

$$\alpha(\omega) = 1 - r(\omega) \quad (3)$$

For the high optical absorption or low reflection, ε_1 and ε_2 should be closer to 1 and 0, respectively ($\varepsilon_2 > 0$). On the other hand, strong surface reflection and low absorption/emission result from significantly large permittivity levels. Since the electric component of light is oriented in the *x-y* plane during normal incidence of incoming photons on the material, the in-plane permittivity (*i.e.*, ε_{xx} and ε_{yy}) predominates in the reflection. It is interesting to note that the peak of the in-plane and out-of-plane ε_1 and ε_2 of MXenes appears close to the mid-IR region before dropping off significantly at higher energies. Typically, V_2C exhibits a change from positive to negative in-plane permittivity values in the NIR region (~2 μm), indicating a strong metallic response to near IR light (Fig. 3a). As a result, V_2C exhibit substantial solar absorption but low IR emission, which is in agreement with the measured spectrum. In the UV–visible-NIR region, both the in-plane and out-of-plane ε_1 and ε_2 are substantially smaller, providing the wavelength selectivity for light absorption.

The absorption/emissivity spectra of MXenes are depicted as a function of wavelength in Fig. 3c. In the considered spectrum range, there are many prominent and less prominent peaks, which are ascribed to the intra- and inter-band transitions. It is preferable to have the well-aligned nano-flakes parallel to the substrate because the absorptance estimated from the in-plane permittivity displays a significantly higher spectral selectivity than that from the *z*-direction. The results show that Ti_3C_2 has ultralow absorption, while V_2C and V_4C_3 show low emissivity in mid-IR range. Nb_2C has a higher IR emissivity than other MXenes, which is consistent with the measured trend, although

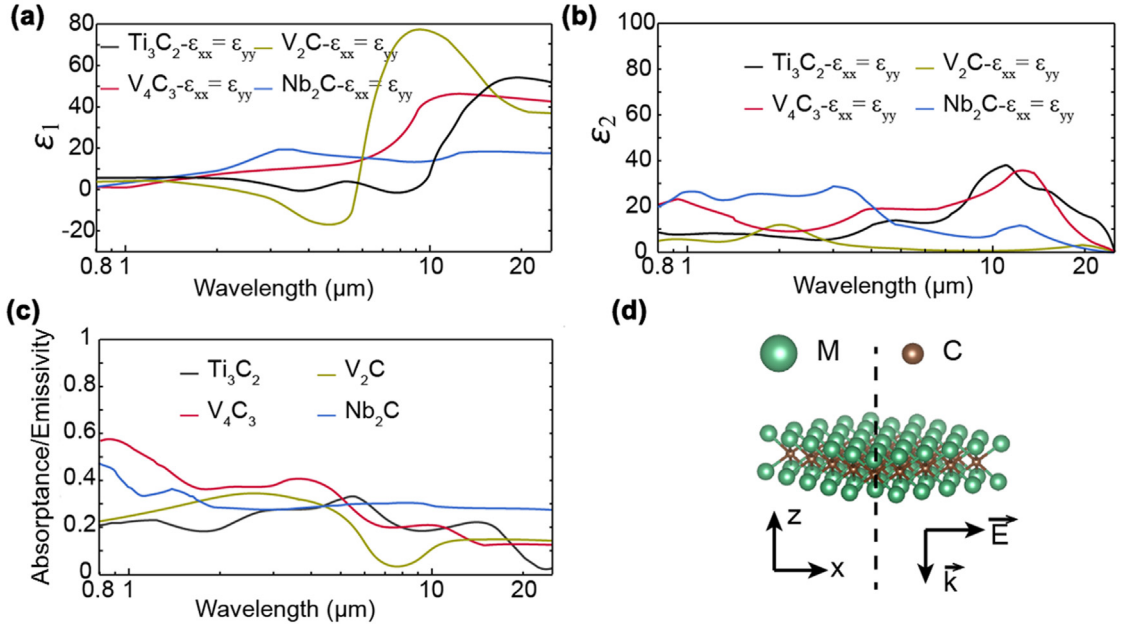

FIGURE 3

DFT calculations. The calculated (a) real and (b) imaginary parts of in-plane permittivity of V_2C, Nb_2C, Ti_3C_2, and V_4C_3 MXenes. (c) Calculated absorptance/emissivity spectra of V_2C, Nb_2C, Ti_3C_2, and V_4C_3 MXenes. (d) A 2D layer structure schematic of MXene, showing the direction of wave vector *k* along the *z*-direction and the electric component of light oriented in the *x-y* plane.

the absolute value is lower than the experimental data. There are two factors that may have a profound impact on the IR radiation but are not considered in the calculations. First, there are defects in MXene flakes after acid-etching and ion/molecule delamination, which change the electron transport and dielectric properties of MXenes [42]. Second, the surface groups (-O, –OH, and -F) have a complicated distribution on the surface. Moreover, it was found that oxygen can be present in the carbon sublattice [43]. All those factors may affect MXene properties, but are difficult to account for in modeling. The fundamental understanding of MXene interaction with IR radiation still needs further investigation and understanding of the role of defects, flake orientation, diffraction, surface terminations, *etc*.

Infrared identification with MXenes

Precise localized imaging and thermal management can be achieved with the MXene family in integrated systems, which is attributed to their diversity in optical and infrared absorptance (effectiveness in absorbing radiant energy). As a proof of concept, we fabricated a circle palette with six MXene films (Ti_2CT_x, $Ti_3C_2T_x$, Ti_3CNT_x, $V_4C_3T_x$, $Nb_4C_3T_x$, and $Mo_2Ti_2C_3T_x$) on polyethylene terephthalate (PET) substrate and placed it on a hot plate at 70 °C to show visible/IR identification. While the palette visually exhibits diverse bright colors with various MXenes, they show very different colors in a distinct order and different temperatures under an IR camera, due to their different IR emissivities (Fig. 4a). It is promising to use different MXenes to load information for security and modulate radiative heating/cooling precisely on demand. Generally, the surface condition of an object has a significant effect on the IR emissivity. We further printed a word 'Drexel' on cotton fabric, where each letter was printed using a different MXene (Fig. S12). Although there was no apparent difference in perceived color due to the diffusive nature of the rough-textured textile, the MXenes can be distinguished under an IR camera. This demonstrates that the MXene coatings have the capability to exhibit wide-range and sensitive IR emission, even on rough, porous, or uneven surfaces (Figs. S13a-13c). More importantly, it indicates that MXenes not only can be used for visual perception but also for object identification/-camouflage. This was demonstrated using a black fabric which patterned with a QR code 'MXene' in dark environment (Fig. 4b). Though the fabric was screen printed with a thick layer of $Ti_3C_2T_x$ MXene (Figs. S13d-13f), the code was indistinguishable with a normal optical camera in the dark environment. In contrast, the information can be quickly recognized with an IR camera (Movie S1). A $Ti_3C_2T_x$-coated T-shirt was made using dip-coating method to show the large-scale manufacturing and IR camouflage capability (Fig. S14). Furthermore, $Ti_3C_2T_x$ and Nb_2CT_x, with the lowest and highest IR emissivity among all tested MXenes, respectively, were spray-coated on fabric with a pattern of dragon (Fig. 4c). Compared with carbon black-coated fabric ($\varepsilon \approx 1$), $Ti_3C_2T_x$-coated fabric appears much cooler (~30 °C) than the background (~60 °C), but Nb_2CT_x-coated fabric shows a similar color. It means that MXenes can be potentially used for both radiative heating and cooling, depending on MXene compositions and structures.

Conclusions

In summary, we have demonstrated that MXenes with different compositions and structures have IR emissivity values ranging from ~ 0.06 to 0.59, covering both low-emission and high-

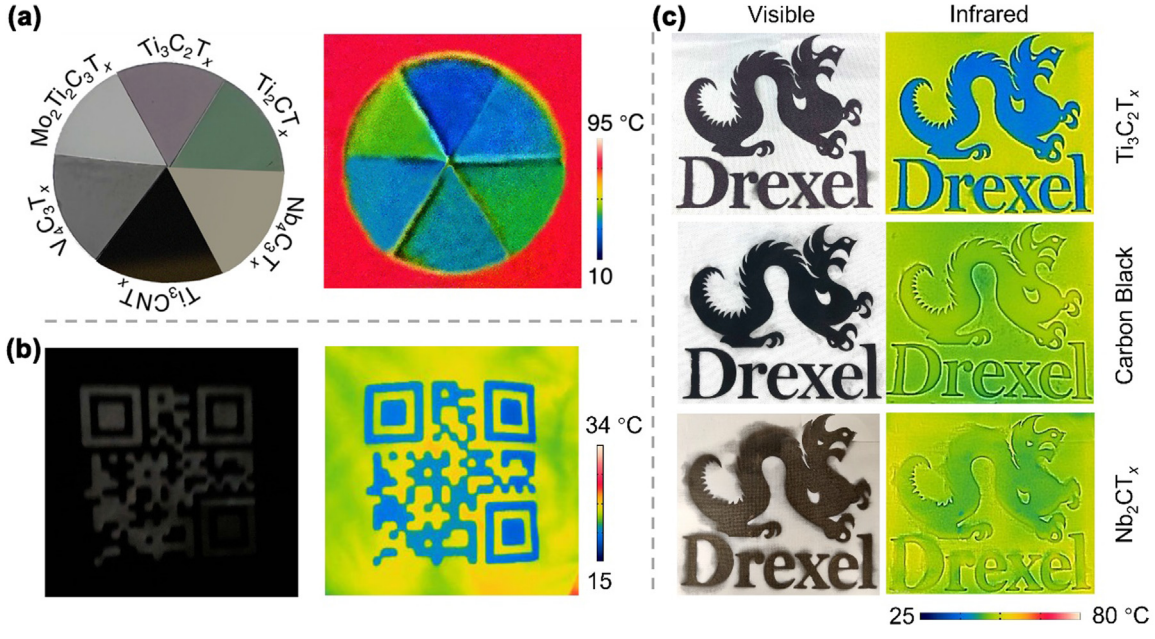

FIGURE 4

Infrared identification with MXenes. (a) Visible (left) and infrared (right) images of different MXene coatings (Ti_2CT_x, $Ti_3C_2T_x$, Ti_3CNT_x, $Nb_4C_3T_x$, $V_4C_3T_x$, and $Mo_2Ti_2C_3T_x$) on a hot plate at 70 °C, showing the identification capability of MXenes due to their varying colors and infrared emissivity. (b) Digital (left) and infrared (right) images of a $Ti_3C_2T_x$-coated black fabric with a QR code of 'MXene' attached on a human body in the dark, showing the infrared identification of $Ti_3C_2T_x$. Details are in Movie S1. (c) Visible (left) and infrared (right) images of MXene-coated fabrics ($Ti_3C_2T_x$ and Nb_2CT_x) on a hot plate compared with a carbon black-coated fabric.

emission ranges. The IR emissivity of MXene films decreases with the increasing electrical conductivity. The evolution from low to high IR emission can be achieved with elemental substitution in solid solution MXenes. The low IR emission of Ti-based MXenes up to 673 K demonstrates their radiation depression capability at high temperatures. We showcased the visible and IR identification capability with various MXene films and MXene-patterned fabrics. The IR radiation properties of MXenes coupled with non-linear optical absorbance in UV–vis-NIR range show the potential of MXenes for integration into wearables and devices with selective IR identification/stealth, imaging, thermal insulation, and localized thermal manipulation.

Materials and methods

Materials

Al (99.5 %, −325 mesh, Alfa Aesar), TiC (99.5 %, ~2 μm, Alfa Aesar), AlN (98 %, 10 μm, Aldrich), Ti (99.5 %, −325 mesh, Alfa Aesar), Nb (99.99 %, −325 mesh, Beantown Chemical), Mo (99.9 %, −250 mesh, Alfa Aesar), V (99.5 %, −325 mesh, Alfa Aesar), C (graphite, 99 %, −325 mesh, Alfa Aesar), HF (48.5–51 %, Acros Organics), HCl (36.5–38 %, Fisher Chemical), LiCl (99 %, Acros Organics), and tetramethylammonium hydroxide (TMAOH; 25 wt%, Acros Organics).

Synthesis of MAX phases

Prior to synthesis, all precursor powders were mixed in the ratios specified in Table 1. The mixture was placed into plastic jars with zirconia balls and ball milled at 50 rpm for 18 h. The powder mixture was transferred to an alumina crucible and was placed into a high temperature furnace. The samples were heated and cooled at a rate of 3 °C/min with Ar continually flowing at 200 ccm. Depending on the chemistry and composition, different temperatures and holding times were used (Table 1). The sintered compact was milled with a TiN coated bit and the produced powder was sieved to < 38 μm. The powders were washed with 9 M HCl for 24 h to remove residual intermetallics and metals and then repeatedly washed with deionized (DI) water to neutral pH.

Synthesis of MXenes

Etching of MXenes. MXenes were synthesized by selective etching of the corresponding MAX phase powders with an acid or acids mixture, depending on MXene composition (details in Table 2). The synthesis procedures were reported in our previous work [20]. For example, 1 g of Nb_2AlC powder was added to 10 mL of HF and stirred for 48 h at room temperature. After etching, the solution was repeatedly centrifuged with DI water at 3500 rpm for 2 min until pH > 6. The obtained sediment was collected for delamination. For MAX phases etched with HF and HCl, 1 g of MAX powder was mixed with 2 mL of HF and 12 mL of HCl.

Delamination of MXenes. Multilayered MXenes were delaminated to obtain colloidal solutions of single- and few-layered MXenes with TMAOH or LiCl, depending on MXene composition (details in Table 2). For example, multilayered Nb_2CT_x was

TABLE 1

The synthesis conditions of MAX phases in this work.

Type	MAX phase	Precursors	Atomic ratio	Annealing temperature (°C)	Annealing time (h)
211	Ti_2AlC	Ti: Al: C	2: 1.1: 0.9	1550	2
	Nb_2AlC	Nb: Al: C	2: 1.1: 0.9	1550	2
	V_2AlC	V: Al: C	2: 1.1: 0.9	1550	2
	$Ti_{0.4}Nb_{1.6}AlC$	Ti: Nb: Al: C	0.4: 1.6: 1.1: 0.9	1550	2
	$Ti_{1.6}Nb_{0.4}AlC$	Ti: Nb: Al: C	1.6: 0.4: 1.1: 0.9	1550	2
312	Ti_3AlC_2	TiC: Al: Ti	2: 2.2: 1.25	1400	2
	Ti_3AlCN	Ti: AlN: C	3: 1: 1	1500	2
413	Nb_4AlC_3	Nb: Al: C	4: 1.1: 2.7	1650	4
	V_4AlC_3	V: Al: C	4: 1.5: 3	1500	2
	$Mo_2Ti_2AlC_3$	Mo: Ti: Al: C	2: 2: 1.3: 2.7	1600	4

TABLE 2

The synthesis conditions of MXenes used in this work.

Type	MXene	Etching reagent	Etching temperature (°C)	Etching time (h)	Delamination reagent
21	Ti_2CT_x	HF, HCl	RT	24	LiCl
	$Ti_{1.6}Nb_{0.4}CT_x$	HF, HCl	35	48	LiCl
	Nb_2CT_x	HF	RT	48	TMAOH
	V_2CT_x				
	$Ti_{0.4}Nb_{1.6}CT_x$				
32	$Ti_3C_2T_x$	HF, HCl	RT	24	LiCl
	Ti_3CNT_x				
43	$Nb_4C_3T_x$	HF	35	168	TMAOH
	$V_4C_3T_x$			192	
	$Mo_2Ti_2C_3T_x$			96	

added to a solution of 0.5 g TMAOH and 10 mL of DI water and stirred for 12 h at room temperature. The mixture was repeatedly centrifuged with DI water at 10000 rpm for 10 min until pH < 8. At last, the swelled sediment was centrifuged at 3500 rpm for 10 min. The supernatant was the dispersion of delaminated Nb_2CT_x flakes in water.

Fabrication of MXene coatings

Spray-coated MXene films. MXene films were fabricated by spray-coating from MXene aqueous solutions. Microscopic glass slides (Fisher Scientific) and cotton fabric were used as the substrates. Before spray-coating, the slide was cleaned by ethanol and DI water with sonication. The pristine cotton fabric was washed using Synnthrapol@, an industrial-strength liquid detergent. The cleaned substrate was plasma-treated (Tergeo Plus, Pie Scientific) at 100 W with oxygen flow at 3 sccm for 5 min. Additive-free MXene colloidal solution was sprayed onto the substrate manually. For the patterned MXene coatings, a mask was placed on the substrate for spray-coating. The sprayed samples were dried in a vacuum oven at 70 °C for 12 h.

MXene-coated fabrics. MXene-coated fabric patterned with a QR code was fabricated using screen printing method. The selected QR code ('*MXene*') was inkjet-printed onto a transparent acetate film. The stencil was fabricated by covering the printed transparent film over a pre-photo-emulsion-coated polyester mesh and passed together through an UV exposure unit (MYSO280, Screen Sensations, USA). The mesh areas right underneath the black QR code were shielded from UV in the process, thus not cured/crosslinked during the UV exposure and could be washed off subsequently with water. The fabricated stencil was line dried before screen printing. The screen printing of concentrated $Ti_3C_2T_x$ ink on cotton fabric (ISO adj cotton, Test Fabrics) was executed with 12 × 12 inches screen printing setup (Screen Sensations, USA) manually and the process was repeated 3 times with thorough drying between print passes. MXene-coated T-shirt was fabricated using a dip-coating method. The clean cotton T-shirt was dipped in an additive-free $Ti_3C_2T_x$ solution and subsequently air dired.

Characterization

The morphology of MXene flakes was observed using scanning electron microscopy (SEM; Zeiss Supra 50VP, Germany). A 3D laser scanning confocal microscopy (Keyence, VK-X1000, Japan) was used to observe the coating surface and measure the coating roughness and thickness. XRD patterns of MAX phases and MXene coatings were measured using a Rigaku SmartLab (Tokyo, Japan) operating at 40 kV/30 mA with Cu Kα radiation. Raman spectra were measured with an inverted reflection mode Renishaw (2008, Gloucestershire, UK) dispersive instrument, equipped with a 63× (NA = 0.7) objective. The excitation wavelength of 633 nm was used and the laser power was kept around 0.1 mW. The infrared images and temperature were recorded using an IR camera (FLIR E8xt, USA). The camera emissivity was set as 0.94. The reflectivity (R) of MXene coatings in the 1–25 μm range at room temperature was measured using a FTIR spectrometer (Invenio-X, Bruker, Germany). The FTIR with a reflectance accessory (10Spec, Pike Technologies) was used to measure the specular reflectance of the smooth spray-coated MXenes films directly. The measurement reference was a gold mirror. The emissivity (ε) was calculated using Kirchhoff's law (ε = 1-R). The high-temperature emissivity was in-situ measured using the FTIR spectrometer via thermal emission. An emission adapter (A540/3) was used to heat the samples and the black body reference (a soot layer on metal sheet). The emissivity in the 3–25 μm range is given by the ratio of sample emission (v) and the reference emission at the same temperature (T). The following was used:

$$\varepsilon(v,T) = \frac{MXene\ emission(v,T)}{Black\ body(v,T)} \quad (4)$$

DFT calculations

All first-principles calculations were performed using the projector-augmented-wave (PAW) approach, which is implemented in the Vienna Ab initio Simulation Package (VASP) [44,45]. The exchange–correlation was completed using the Perdew-Burke-Ernzerhof (PBE) generalized gradient approximation [46] for relaxing the atomic positions and the Heyd-Scuseria-Ernzerhof (HSE06) [40] hybrid exchange–correlation functional was used for all following calculations. The kinetic energy cutoff of the plane-wave basis was set to 600 eV. The structural optimization is performed until the remaining forces on the atoms are less than 0.005 eV/Å. The unit cell of Ti_3C_2, V_4C_3, V_2C, and Nb_2C is optimized using a dense Monkhorst-Pack k-point grid (21 × 21 × 1).

Author contributions

M.H. and Y.G. conceived this study. M.H., D.Z., and T.H. designed and performed the IR measurements. M.H., D.Z., and B.M. synthesized MXenes. M.H., D.Z., T.H., and L.B. fabricated MXene films and coatings. A.S. and V.B.S. performed the calculations. C.S. synthesized MAX phases and performed XRD measurements. T.Z. performed SEM observation. M.H. wrote the manuscript, with input from all co-authors under supervision from Y.G.

CRediT authorship contribution statement

Meikang Han: Conceptualization, Methodology, Investigation, Writing – original draft, Writing – review & editing, Funding acquisition. **Danzhen Zhang:** Methodology, Investigation, Writing – original draft, Writing – review & editing. **Akash Singh:** Formal analysis, Writing – original draft, Writing – review & editing. **Tetiana Hryhorchuk:** Methodology, Investigation, Writing – review & editing. **Christopher Eugene Shuck:** Investigation, Writing – review & editing. **Teng Zhang:** Investigation, Writing – review & editing. **Lingyi Bi:** Investigation, Writing – review & editing. **Bernard McBride:** Investigation, Writing – review & editing. **Vivek B. Shenoy:** Formal analysis, Writing – review & editing, Supervision. **Yury Gogotsi:** Conceptualization, Supervision, Funding acquisition, Writing – review & editing.

Data availability

Data will be made available on request.

Declaration of Competing Interest

The authors declare the following financial interests/personal relationships which may be considered as potential competing interests: The work is subjected to a patent application (17/782,234) by M.H. and Y.G. The authors declare no other conflict of interest.

Acknowledgements

This work was supported by the U.S. National Science Foundation (grants ECCS-2034114 and DMR-2041050). M.H. acknowledges the support from Shanghai Pujiang Program (22PJ1400800). We thank Dr. Sergey Shilov (Bruker Scientific, *LLC*) for his assistance with preliminary emissivity measurement of MXene coatings. XRD and SEM analyses were performed using instruments in the Materials Characterization Core at Drexel University.

Appendix A. Supplementary material

Supplementary data to this article can be found online at https://doi.org/10.1016/j.mattod.2023.02.024.

References

[1] T. Li et al., Science 364 (2019) 760.
[2] Y. Peng et al., Nat. Sustain. 5 (2022) 339.
[3] X. Yin et al., Science 370 (2020) 786.
[4] Q. Zhang et al., Nat. Commun. 13 (2022) 4874.
[5] E.A. Goldstein et al., Nat. Energy 2 (2017) 17143.
[6] Z. Huang et al., Thin Solid Films 519 (2011) 3100.
[7] Y. Li et al., Nat. Rev. Mater. 6 (2021) 488.
[8] T. Inoue et al., Nat. Mater. 13 (2014) 928.
[9] J. Xu et al., Science 372 (2021) 393.
[10] P.N. Dyachenko et al., Nat. Commun. 7 (2016) 11809.
[11] S. Vassant et al., Appl. Phys. Lett. 102 (2013) 081125.
[12] H. Demiryont, D. Moorehead, Sol. Energy Mater. Sol. Cells 93 (2009) 2075.
[13] M. Han et al., J. Am. Chem. Soc. 142 (2020) 19110.
[14] A. VahidMohammadi et al., Science 372 (2021) eabf1581.
[15] D. Zhang et al., ACS Photonics 9 (2022) 1108.
[16] A. Iqbal et al., Science 369 (2020) 446.
[17] G. Valurouthu et al., Nanoscale 12 (2020) 14204.
[18] G. Li et al., Nano Lett. 20 (2020) 636.
[19] K. Maleski et al., Adv. Opt. Mater. 9 (2020) 2001563.
[20] M. Han et al., ACS Nano 14 (2020) 5008.
[21] M. Han et al., Nat. Nanotechnol. (2023), https://doi.org/10.1038/s41565-022-01308-9.
[22] G. Choi et al., Adv. Opt. Mater. 6 (2018) 1701076.
[23] Y. Li et al., Adv. Mater. 33 (2021) 2103054.
[24] X. Zhao et al., ACS Nano 14 (2020) 8793.
[25] K. Li et al., Adv. Energy Mater. 9 (2019) 1901687.
[26] S. Hong et al., ACS Nano 14 (2020) 9042.
[27] X. Li et al., Research 2022 (2022) 9892628.
[28] M. Shekhirev et al., Prog. Mater. Sci. 120 (2021) 100757.
[29] M. Han et al. 2105.04011, arXiv (2021), https://doi.org/10.48550/arXiv.2105.04011.
[30] Y. Gogotsi, B. Anasori, ACS Nano 13 (2019) 8491.
[31] G. Deysher et al., ACS Nano 14 (2020) 204.
[32] L. Li et al., Adv. Funct. Mater. 31 (2021) 2101381.
[33] S. Pinilla et al., Nat. Rev. Mater. 7 (2022) 717.
[34] S. Abdolhosseinzadeh et al., Mater. Today 48 (2021) 214.
[35] M.S. Ergoktas et al., Nat. Photonics 15 (2021) 493.
[36] X.A. Zhang et al., Science 363 (2019) 619.
[37] J. Szczyrbowski et al., Sol. Energy Mater. 19 (1989) 43.
[38] A. Narayanaswamy, G. Chen, Annu. Rev. Heat Transf. 14 (2005) 169.
[39] F. Ureña-Begara et al., Appl. Surf. Sci. 403 (2017) 717.
[40] J. Heyd et al., J. Chem. Phys. 118 (2003) 8207.
[41] J.E. Sipe, E. Ghahramani, Phys. Rev. B 48 (1993) 11705.
[42] M. Han et al., Cell Rep. Phys. Sci. 3 (2022) 101073.
[43] P.P. Michałowski et al., Nat. Nanotechnol. 17 (2022) 1192.
[44] G. Kresse, J. Furthmüller, 2D Mater. 6 (1996) 15.
[45] G. Kresse, J. Furthmüller, Phys. Rev. B 54 (1996) 11169.
[46] J.P. Perdew et al., Phys. Rev. Lett. 77 (1996) 3865.

Supplementary Information

Versatility of infrared properties of MXenes

Meikang Han[1,2#]*, Danzhen Zhang[1#], Akash Singh[3#], Tetiana Hryhorchuk[1], Christopher Eugene Shuck[1], Teng Zhang[1], Lingyi Bi[1], Bernard McBride[1], Vivek B. Shenoy[3], Yury Gogotsi[1]*

[1]A. J. Drexel Nanomaterials Institute and Department of Materials Science and Engineering, Drexel University, Philadelphia, PA 19104, USA

[2]Institute of Optoelectronics and Shanghai Frontiers Science Research Base of Intelligent Optoelectronics and Perception, Fudan University, Shanghai 200433, China

[3]Department of Materials Science and Engineering, University of Pennsylvania, Philadelphia, Pennsylvania 19104, USA

*Correspondence to Yury Gogotsi (gogotsi@drexel.edu) and Meikang Han (mkhan@fudan.edu.cn)

[#]These authors contributed equally to this work.

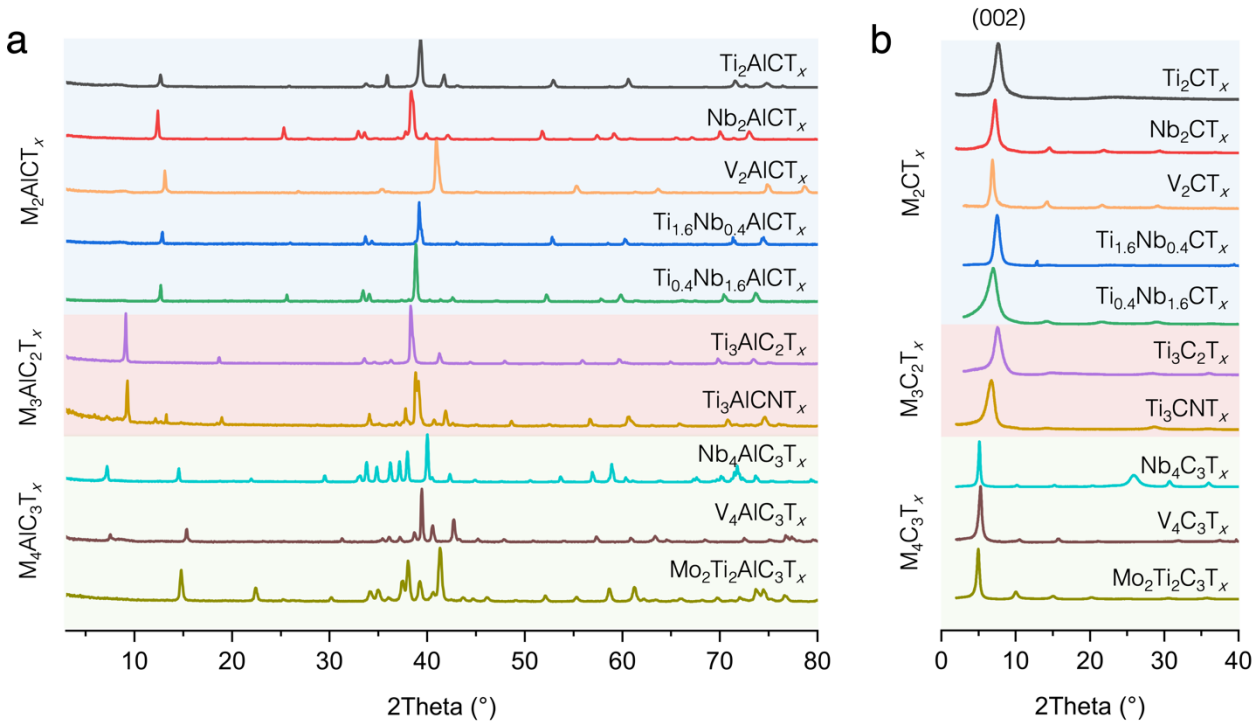

Fig. S1. XRD patterns of (a) MAX phases and (b) MXene films.

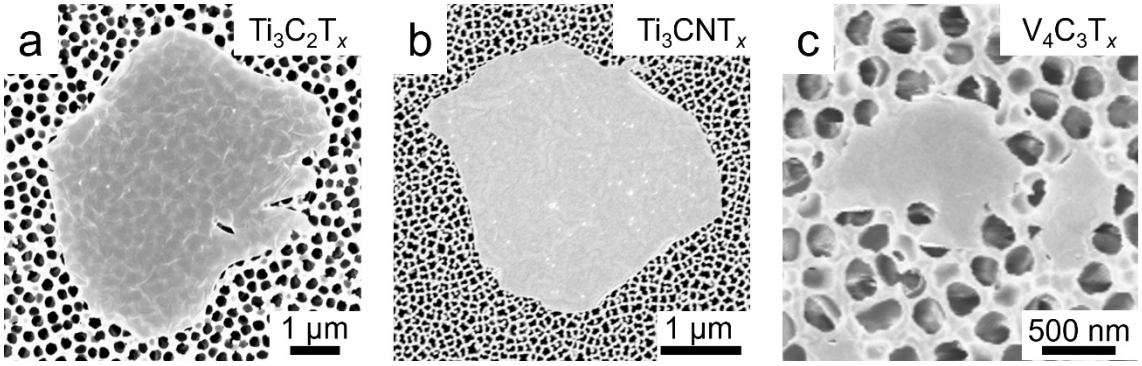

Fig. S2. SEM images of three MXene flakes: (a) $Ti_3C_2T_x$, (b) Ti_3CNT_x, and (c) $V_4C_3T_x$.

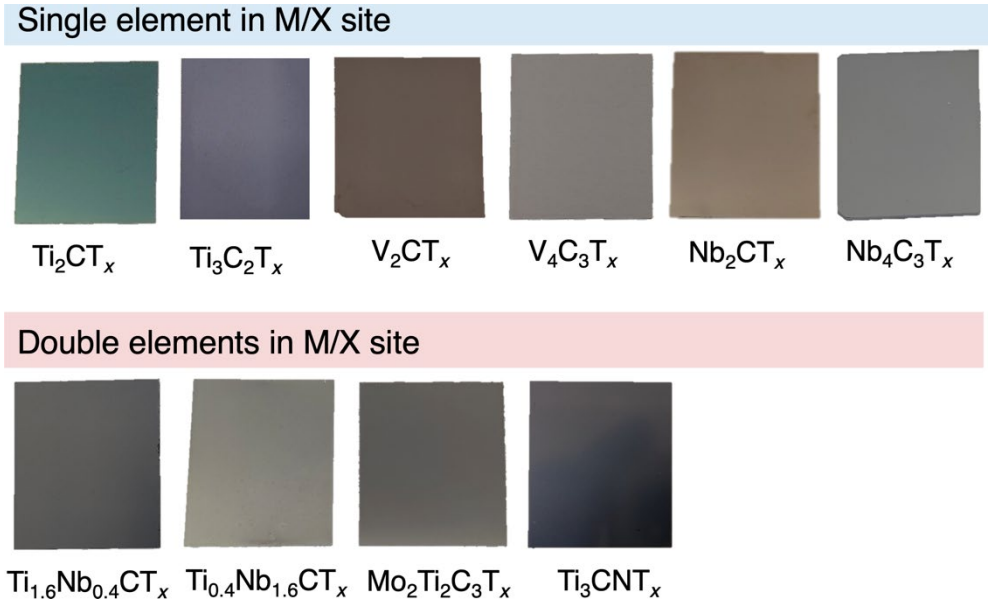

Fig. S3. Digital images of different MXene coatings on glass substrates, showing the smooth surface with different colors.

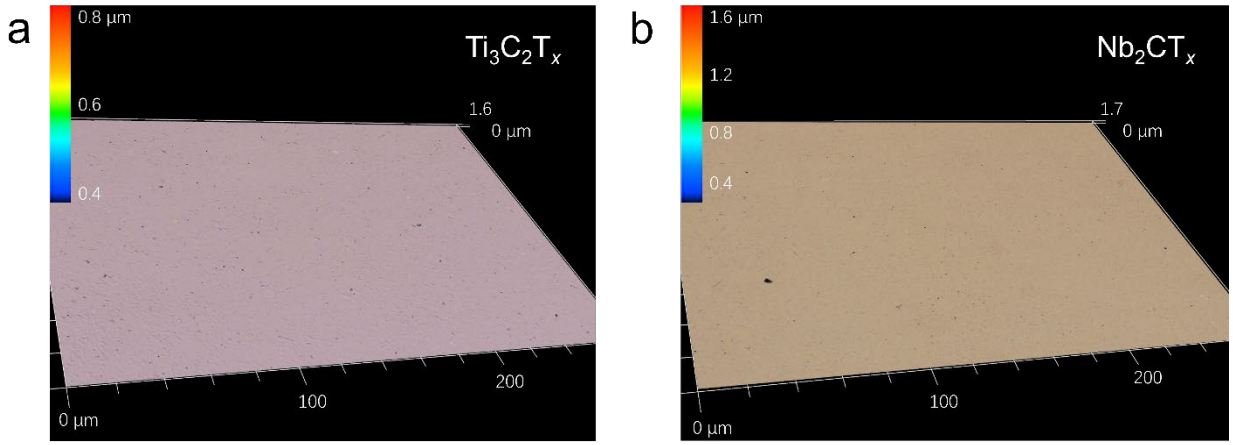

Fig. S4. Optical profilometry maps of (a) $Ti_3C_2T_x$ and (b) Nb_2CT_x coatings showing the surface roughness. 18±2 nm for $Ti_3C_2T_x$ and 33±3 nm for Nb_2CT_x.

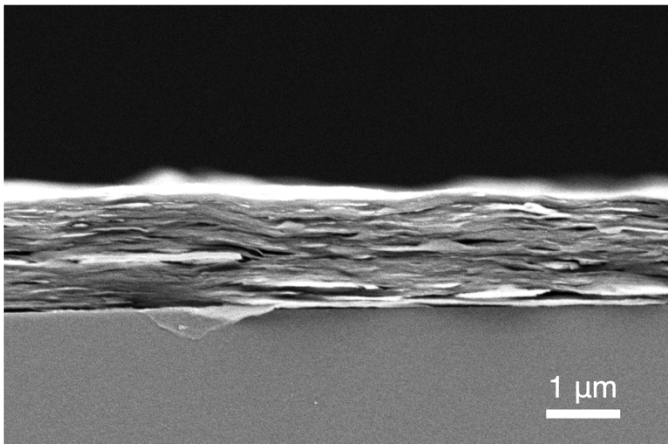

Fig. S5. SEM image of the cross-section of a MXene coating on glass substrate, showing the well aligned layers.

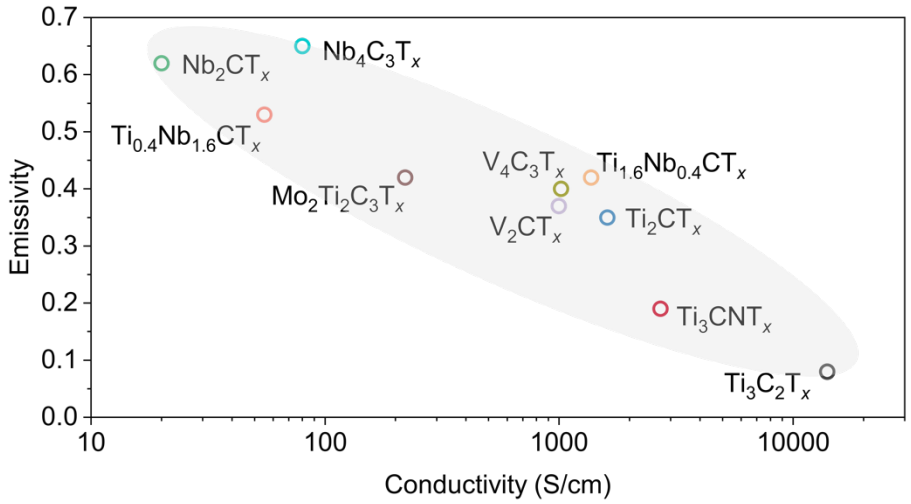

Fig. S6. The relationship between the average infrared emissivity (3-5 µm range) and electrical conductivity of MXene coatings.

Table S1. Comparison of IR emissivity between MXene films and other films (metal films and transparent films) in the literature.

Materials	IR emissivity	Thickness (nm)	Wavelength (μm)	Ref.
$Ti_3C_2T_x$	0.047	200	8-14	This
Nb_2CT_x	0.59	200	8-14	work
Al-doped ZnO (AZO) film	0.41	500	8-14	[1]
TiN_x film	0.1	577	8-14	[2]
Au film	0.05 0.03	200 1000	3-14	[3]
Au/Ni film	0.01	Au:500 Ni:200	3-14	[4]
Indium tin oxide (ITO) film	0.16	600	8-14	[5]
Mo/TiN film	0.03-0.15	Mo:200 TiN:200	3-20	[6]
Pt film	~0.05	500	3-14	[7]
ZrB_2	0.05 0.01	330	3-5 8-14	[8]
Ag/ZrB_2	0.11 0.04	400	3-5 8-14	[9]
Al/SiO_2	0.12	172	8-14	[10]
Ag nanowires film	~0.1	>120	4-15	[11]
Ag/Ge film	0.18 0.31	Ag:50 Ge:953	3-5 8-14	[12]
Ta film	0.28	230	1-3	[13]

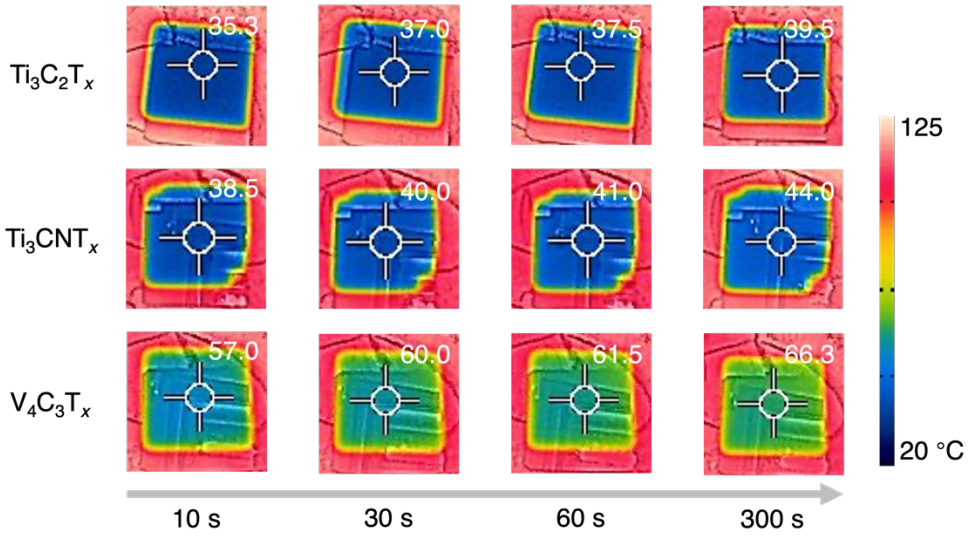

Fig. S7. Infrared images of different MXene coatings ($Ti_3C_2T_x$, Ti_3CNT_x, and $V_4C_3T_x$) on a hot plate at 110 °C recorded at different times.

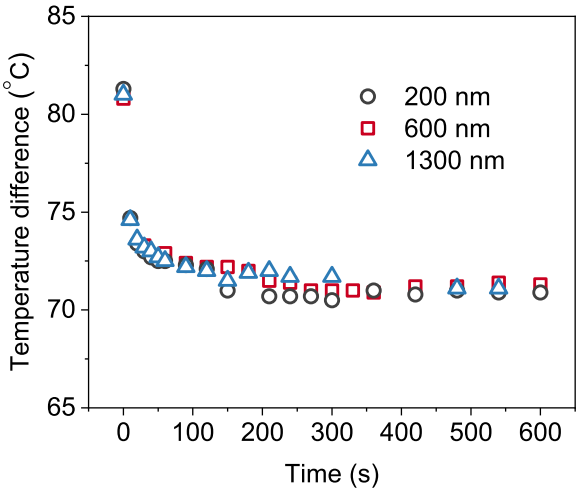

Fig. S8. Temperature difference between MXene coating and background as a function of time for $Ti_3C_2T_x$ coatings with different thicknesses on a hot plate at 110 °C.

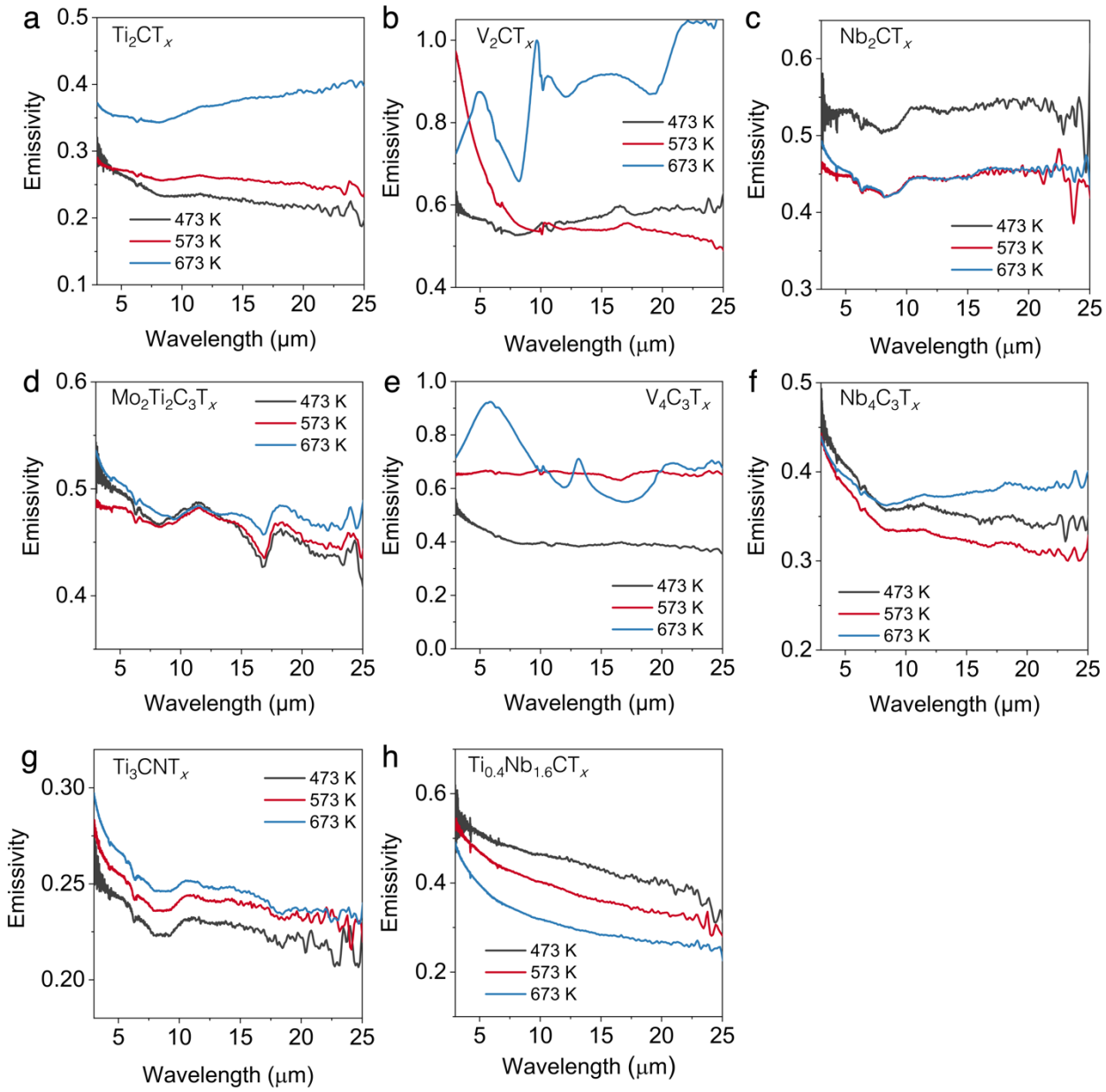

Fig. S9. The infrared emissivity spectra (3-25 μm) at high temperatures (473-673 K) of (a) Ti_2CT_x, (b) V_2CT_x, (c) Nb_2CT_x, (d) $Mo_2Ti_2C_3T_x$, (e) $V_4C_3T_x$, (f) $Nb_4C_3T_x$, (g) Ti_3CNT_x, and (h) $Ti_{0.4}Nb_{1.6}CT_x$ coatings.

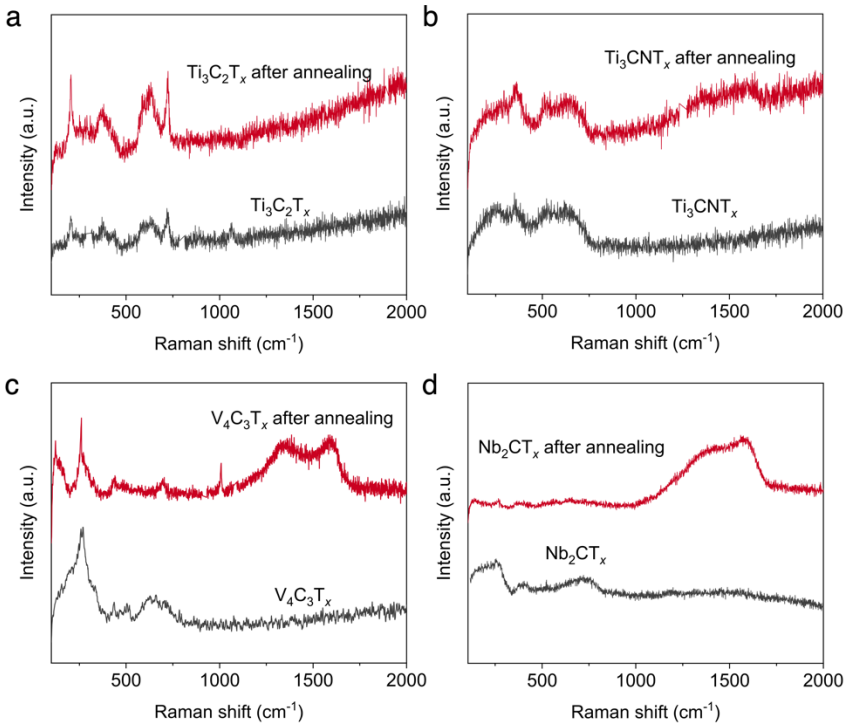

Fig. S10. Raman spectra of MXene coatings before and after infrared testing in the chamber at 673 K. (a) $Ti_3C_2T_x$, (b) Ti_3CNT_x, (c) $V_4C_3T_x$, and (d) Nb_2CT_x. Broad peaks around 1350 and 1600 cm^{-1} show the formation of disordered free carbon.

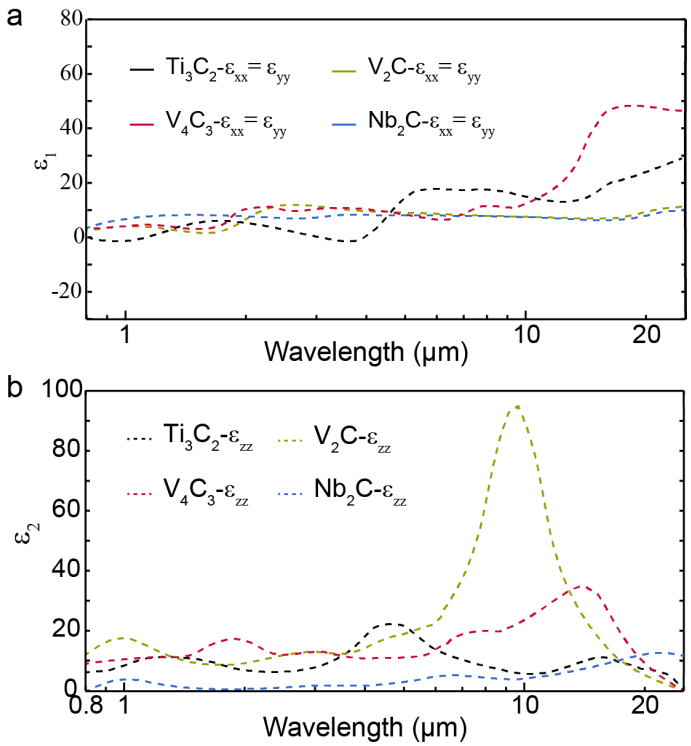

Fig. S11. The calculated (a) real and (b) imaginary parts of out-of-plane permittivity of bare V_2C, Nb_2C, Ti_3C_2, and V_4C_3.

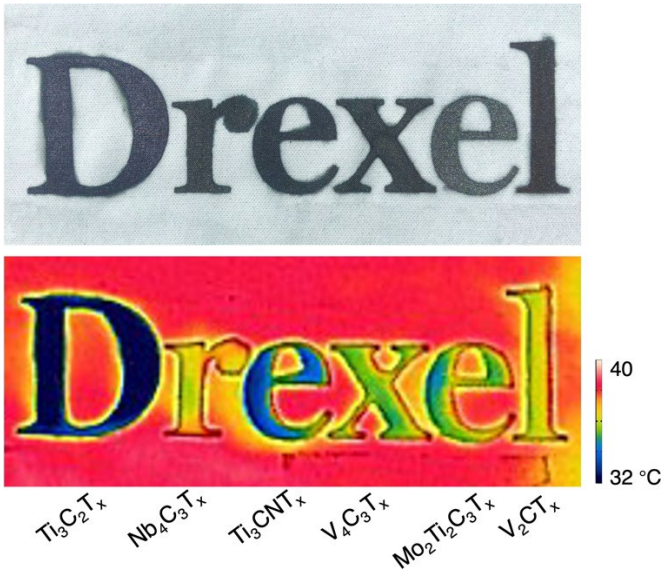

Fig. S12. Visible (top) and infrared (bottom) images of patterned fabric with different MXenes ($Ti_3C_2T_x$, $Nb_4C_3T_x$, Ti_3CNT_x, $V_4C_3T_x$, $Mo_2Ti_2C_3T_x$, and V_2CT_x) on a hot plate, showing the IR identification capability of MXenes.

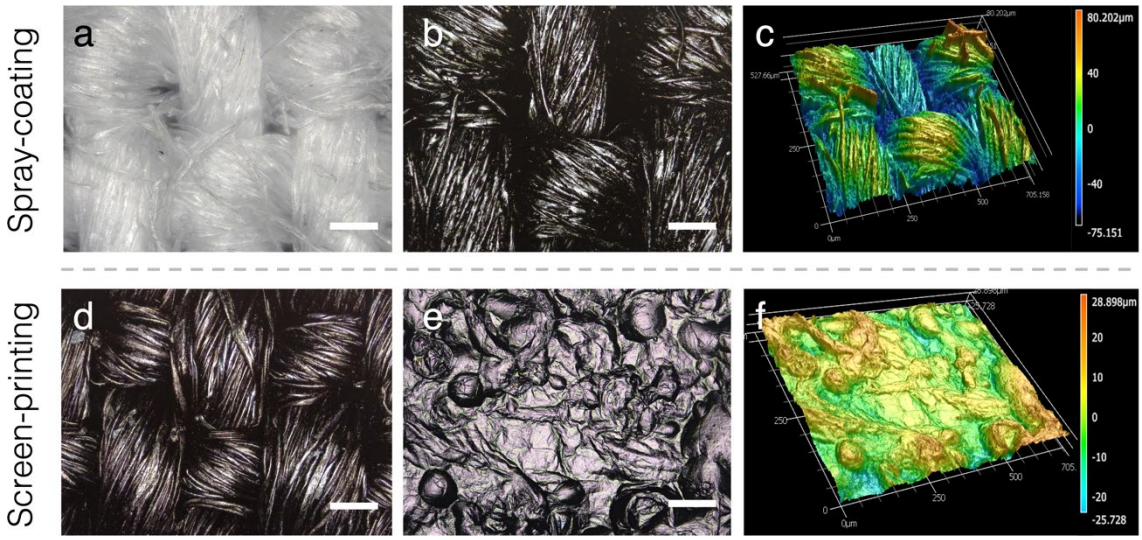

Fig. S13. Optical images of fabrics coated with MXene using different methods. *Spray-coated fabric*: (a) original white fabric; (b) fabric with spray-coated $Ti_3C_2T_x$; (c) optical profilometry map. *Screen-printed fabric*: (d) original black fabric; (e) fabric with screen-printed $Ti_3C_2T_x$; (f) optical profilometry maps.

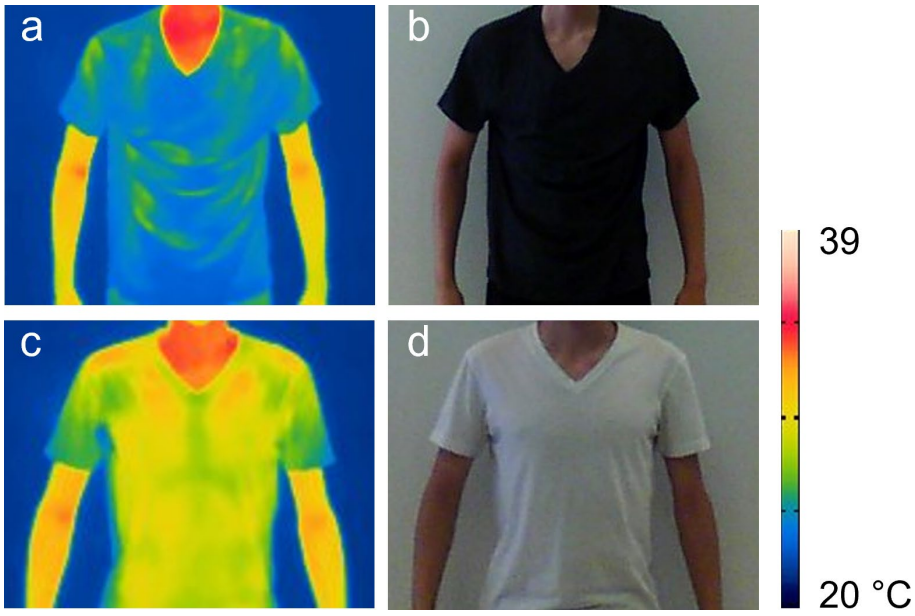

Fig. S14. (a) Infrared and (b) digital images of a $Ti_3C_2T_x$-coated T-shirt fabricated using a dip-coating method, showing the IR camouflage capability of MXene in garment. (c) Infrared and (d) digital images of a normal T-shirt as a reference.

Reference

1. Sun, K., *et al.*, Ceram. Int., 44 (2018), 19597
2. Xu, J., *et al.*, Infrared Phys. Techn., 119 (2021), 103946
3. Huang, Z., *et al.*, Thin Solid Films, 519 (2011), 3100
4. Huang, Z., *et al.*, Appl. Surf. Sci., 256 (2010), 6893
5. Sun, K., *et al.*, Appl. Surf. Sci., 257 (2011), 9639
6. Sun, B., *et al.*, Appl. Surf. Sci., 571 (2022), 151368
7. Huang, Z., *et al.*, Appl. Surf. Sci., 256 (2010), 2025
8. Zhang, M., *et al.*, Appl. Surf. Sci., 527 (2020), 146763
9. Zhang, M., *et al.*, Appl. Surf. Sci., 604 (2022), 154626
10. Chen, L., *et al.*, Opt. Commun., 482 (2021), 126608
11. Pantoja, E., *et al.*, Nanotechnology, 28 (2017), 505708

12. Peng, L.*, et al.*, Adv. Opt. Mater., 6 (2018), 1801006

13. Rinnerbauer, V.*, et al.*, J. Vac. Sci. Technol., 31 (2013), 011501